Effect of grain boundary energy anisotropy on highly-textured grain structures studied by phase field simulations

Kunok Chang[a,b], Nele Moelans[a]

[a] *Department of Metallurgy and Materials Engineering, Katholieke Universiteit Leuven, Kasteelpark Arenberg 44, box 2450, B-3001 Heverlee, Belgium*
[b] *Nuclear Materials Division, Korea Atomic Energy Research Institute (KAERI), 989-111 Daedeok-daero, Yuseong-gu, Daejeon, 305-353, Korea*

Abstract

Two-dimensional phase field simulations were performed of grain growth in highly textured materials with equal fractions of 2 texture components, denoted as α and β grains, and assuming 2 values of the grain boundary energies, namely σ_{low} for the boundaries between grains of a different texture component and σ_{high} for boundaries between grains of a similar orientation, resulting in microstructures with alternating α and β grains and stable quadruple junctions. For different magnitudes of the anisotropy in grain boundary energy $R = \sigma_{high}/\sigma_{low}$, the occurrence of the different types of triple and quadruple junctions and the distributions of the normalized grain size, the number of faces per grain, the normalized grain boundary length per grain and the dihedral angles at grain boundary junctions were investigated.

Keywords: Grain growth, Phase-field modeling, Textured microstructure

1. Introduction

In order to predict various macroscopic properties of polycrystalline materials, characterization of the microstructural characteristics is an essential step[1–4]. For instance, the average grain size plays an important role in determining the yield strength[1, 2] of a material. The evolution of grain structures has been simulated frequently and has been quantitatively characterized by means of the average grain size, the grain size distribution and the number of faces and their distribution [5–7] for isotropic grain boundary properties. Grain growth in anisotropic systems has been simulated based on a Monte Carlo Potts model [8, 9] and using the phase-field method [10]. In their studies, the role of anisotropy in grain boundary energy and mobility in determining the grain size distribution, the distribution of the number of faces per grain and the misorientation distribution of the grain boundaries was evaluated. They assumed that the crystallographic orientations were randomly assigned. Recently, it was also shown that the characteristics of triple and higher order junctions are important

microstructural features in anisotropic systems in the context of grain topology and the misorientation distribution of the grain boundaries[11].

Highly-textured materials are also widely-used [12, 13]. Grain growth of textured materials has been investigated in terms of the distributions of the grain sizes and crystallographic orientations[14, 15]. Moreover, Cahn, Holm and Srolovitz have analyzed the stabilities of trijunctions and quadrijunctions in conserved and non-conserved 2-dimensional two-phase microstructures as a function of the ratios between the grain boundary energies of the different types of interfaces [16, 17], where a system with 2 texture components can be considered as a non-conserved two-phase system. Their study shows that quadruple junctions can become stable for a high degree of anisotropy in grain boundary energy. Different from triple junction dihedral angles, quadruple junction dihedral angles are thermodynamically not fixed, but can vary within a certain range depending on the ratios of the grain boundary energies. They are therefore expected to affect the grain growth behavior and grain boundary network topology considerably. However, in general, the microstructural characteristics of highly-textured materials and the effect of the degree in anisotropy in grain boundary energy in these systems have not been studied extensively. Moreover, very little attention has been given so far to characterize the different possible types of vertices and the distribution of dihedral angles in highly anisotropic systems.

In this paper, we present a systematic study of the role of degree of anisotropy in grain boundary energy in determining the occurrence of different types of vertices, the dihedral angle distribution and the distributions of the number of faces, grain boundary length and grain size in highly-textured materials for microstructures with 2 texture components. The grains belonging to the 2 different components will be labeled respectively as α and β grains. We will consider the case where $\sigma_{\alpha\beta} = \sigma_{low} \leq \sigma_{\alpha\alpha} = \sigma_{\beta\beta} = \sigma_{high}$ with $\sigma_{\alpha\beta}, \sigma_{\alpha\alpha}$ and $\sigma_{\beta\beta}$ the interfacial energy of the boundaries between α grain-β grain, α grain-α grain and β grain-β grain, respectively, for which quadruple junctions have been predicted to coexist with triple junctions and even become the majority junction type within certain ranges of the degrees of anisotropy [16]. This situation is less common than the opposite case where $\sigma_{\alpha\beta} > \sigma_{\alpha\alpha} = \sigma_{\beta\beta}$ for the classical metallic systems (Al, Ni, Cu, ... alloys) with a simple face centered or body centered cubic structure. However, in more complex non-cubic structures, such as monoclinic zirconia [18] and ferroelectric $Cd_{1-x}Zn_xTe$ (CZT) [19], where multiple twin systems may exist, mosaic-like grain structures with only 2 texture components and quadruple junctions where almost perfect twin boundaries (with extremely low energy) and low angle boundaries meet, were observed. The case where $\sigma_{\alpha\beta} > \sigma_{\alpha\alpha} = \sigma_{\beta\beta}$ has been studied before[14, 17, 20] and it was found that the topological characteristics are quite similar to those of isotropic systems since only triple junctions can be stable. The grain growth kinetics can however deviate strongly from those observed for isotropic grain structures. Depending on the initial fractions of the α and β texture components and their initial spatial distribution, the steady-state parabolic growth regime as derived for isotropic grain growth [21–23] may not be obtained.

For the simulated microstructures, we will verify five of the findings in ref. [16, 17] :

1. For isotropic grain growth ($\sigma_{low} = \sigma_{high}$), quadrijunction or higher grain junctions are unstable and unlikely ever to form. Even though they form, they decompose immediately.
2. The $q_{\alpha\beta\alpha\beta}$ type of quadrijunction becomes stable when $R(= \sigma_{high}/\sigma_{low}) \geq \sqrt{2}$. When $\sqrt{2} \leq R \leq \sqrt{3}$, $q_{\alpha\beta\alpha\beta}$ quadrijunctions and trijunctions coexist. Although $t_{\alpha\alpha\alpha}$ and $t_{\beta\beta\beta}$ trijunctions can be stable, $t_{\alpha\alpha\beta}$ and $t_{\alpha\beta\beta}$ trijunctions are thermodynamically more favorable.
3. When $\sqrt{3} < R$, $t_{\alpha\alpha\alpha}$ and $t_{\beta\beta\beta}$ trijunctions become unstable. For $\sqrt{3} < R < 2$, $t_{\alpha\alpha\beta}$ and $t_{\alpha\beta\beta}$ trijunctions coexist with $q_{\alpha\beta\alpha\beta}$ quadruple junctions.
4. Only $q_{\alpha\beta\alpha\beta}$ quadrijunctions are stable when $R \geq 2$.

Following the notation of ref. [16, 17], $t_{\alpha\alpha\beta}$ is a triple junction where 2 α and 1 β grain coexist and a similar notation is used for the 3 other kinds of triple junctions. $q_{\alpha\beta\alpha\beta}$ is a quadruple junction where 2 α and 2 β grains meet according to a checkerboardpattern. Other kinds of quadruple junctions have been shown to be unstable [16, 17].

Furthermore, the distributions of grain sizes, average number of faces per grain, dihedral angles and grain boundary length per grain will be characterized and the findings will be related to the stability of (a) particular type(s) of junctions. Since it is extremely complex to determine and classify uniquely dihedral angles in 3-dimensional systems, 2-dimensional simulations were performed. Although some of the phenomena present in 3-dimensional systems may not be present in 2-dimensional systems, the 2-dimensional simulations can already provide useful insights. They may also represent grain growth behavior in thin films, as that observed for the monoclininc zirconia or $Cd_{1-x}Zn_xTe$ (CZT) thin films. Moreover, the results from our 2-dimensional simulations can be interpreted based on the analytical theory of Cahn [16] which was also for 2-dimensional systems.

2. Phase-field model and numerical solution

We adopted the multi-order parameter phase-field grain growth model of ref. [5]. According to ref. [5], a single-phase material is represented by a set of non-conserved order parameters, which are a continuous function of time and space

$$\eta_1(\mathbf{r}, t), \eta_2(\mathbf{r}, t), ..., \eta_Q(\mathbf{r}, t) \tag{1}$$

Each grain is represented by a unique non-conserved order parameter. The temporal and spatial evolution of the order parameters is described by the time-dependent Ginzburg-Landau equation.

$$\frac{\partial \eta_i(\mathbf{r}, t)}{\partial t} = -L \frac{\delta F}{\delta \eta_i(\mathbf{r}, t)} \tag{2}$$

where the kinetic constant L is related to the grain boundary mobility and the free energy F is a function of the order parameter values and their gradients:

$$F = \int_V \left[\sum_i^Q \left(\frac{\eta_i^4}{4} - \frac{\eta_i^2}{2} \right) + \sum_i^Q \sum_{i \neq j}^Q \theta_{ij} \eta_i^2 \eta_j^2 + \frac{\kappa}{2} \sum_i^Q (\nabla \eta_i)^2 \right] dV \tag{3}$$

The parameters θ_{ij} and κ in the free energy functional determine the grain boundary energies and magnitude of grain boundary energy anisotropy. The grain boundary energy of a boundary between grains i and j is given by the following integral expression [24]

$$\sigma = \int_{-\infty}^{+\infty} \left[\sum_{k=i,j} \left(\frac{\eta_k^4}{4} - \frac{\eta_k^2}{2} \right) + \theta_{ij} \eta_i^2 \eta_j^2 + \frac{\kappa}{2} \left(\left(\frac{d\eta_i}{dx} \right)^2 + \left(\frac{d\eta_j}{dx} \right)^2 \right) \right] dx \tag{4}$$

with x measured perpendicular to the grain boundary. Its value was obtained by numerical integration over the equilibrated order parameter profiles across a straight grain boundary. A similar model was used by Tang et al. [25]. They showed that this model can reproduce the dihedral angles in highly anisotropic systems with high accuracy.

To solve equations (2), a bounding box algorithm [26, 27] is implemented in 2-D in combination with a semi-implicit spectral method [28]. The use of a semi-implicit discretization scheme allows us to take considerably longer discretized time steps (Δt) than is possible with the standard explicit discretization scheme. The bounding box algorithm is based on a sparse data structure and has proven to reduce considerably the computational requirements for large-scale grain growth simulations. In contrast to other sparse data structure algorithms [29, 30] developed for phase-field models, the bounding box algorithm can be combined with implicit and semi-implicit time stepping schemes. The time derivative in equations (2) is discretized using a first-order semi-implicit scheme [28], in which the homogeneous energy part is treated explicitly and the gradient energy part implicitly:

$$\frac{\eta_i^{n+1} - \eta_i^n}{\Delta t} = L \left[(\kappa \nabla^2 \eta_i)^{n+1} + \left[\eta_i^3 + \eta_i - 2\theta_{ij} \eta_i \left(\sum_j^Q \eta_j^2 \right) \right]^n \right], i = 1, 2, ..., Q \tag{5}$$

Let's define $\phi^n(\mathbf{r}) = \left[\eta_i^3 + \eta_i - 2\theta_{ij} \eta_i \left(\sum_j^Q \eta_j^2 \right) \right]^n$. $\tilde{\phi}^n(\mathbf{k})$ and take $\tilde{\eta}^n(\mathbf{k})$ to represent the Fourier transforms of $\phi^n(\mathbf{r})$ and $\eta^n(\mathbf{r})$, respectively. By transforming the partial differential equations (5), we get a sequence of ordinary differential equations in the Fourier space :

$$\frac{d\tilde{\eta}_i^n(\mathbf{k})}{dt} = L[\tilde{\phi}^n(\mathbf{k}) - \kappa k^2 \tilde{\eta}_i^n(\mathbf{r})], \tag{6}$$

where $k = \sqrt{k_1^2 + k_2^2}$ is the magnitude of $\mathbf{k}$, a vector in the Fourier space. The

left hand side of equation (6) is approximated by a forward Euler scheme giving,

$$\tilde{\eta}_i^{n+1}(\mathbf{k}) = \frac{\tilde{\eta}_i^n(\mathbf{k}) + L\Delta t\tilde{\phi}^n(\mathbf{k})}{1 + L\Delta t\kappa k^2} \tag{7}$$

In the bounding box algorithm, a cuboid region is defined around each grain i and for η_i the equation (7) is only solved for the grid points within this region. In our study, each order parameter indicates only one grain in the system. Therefore, the non-physical grain coalescence observed in [5] is entirely eliminated.

$R = \sigma_{high}/\sigma_{low}$	θ_1	θ_2
1.00	1.000	1.000
1.39	1.400	0.700
1.67	1.300	0.620
1.81	1.350	0.600
3.10	1.325	0.530

Table 1: The ratios between grain boundary energies $R = \sigma_{high}/\sigma_{low}$ and associated θ_1 and θ_2 values used in this study.

To simulate grain growth in a highly-textured material, we will assume that all grains with i even belong to the α variant and all grains with i uneven to the β variant. To introduce the two different grain boundary energies, with σ_{high} for the boundaries between grains with a similar orientation and σ_{low} for the boundaries between grains of a different orientation, $\theta_{ij} = \theta_1$ is set in equation (3) when $i + j$ is even and $\theta_{ij} = \theta_2$ is set otherwise. The θ_{ij} values and the corresponding ratio, between the grain boundary energies $R = \sigma_{high}/\sigma_{low}$ used in this study are listed in Table 1. Furthermore, we choose $L = 1.0$, $\kappa = 2.0$ and the time step is taken $\Delta t = 1.0$ and $\Delta x = \Delta y$ is 2.0. All lengths and times will be expressed in multiples of Δx (voxel) and Δt (time step).

3. Determination of multiple junctions, grain boundary length and dihedral angles

We implemented a new methodology to classify the multiple junctions and measure the dihedral angles at multiple junctions from the voxel based microstructure representations obtained from the phase-field simulations. Moreover, an improved iterative method to measure grain boundary length in the voxel based microstructure representation is developed.

3.1. Classification of the multiple junctions and measurement of dihedral angles

The procedure implemented to find and classify the multiple junctions and measure their dihedral angles in the voxel based microstructure representation is described below and illustrated in Fig. 1.

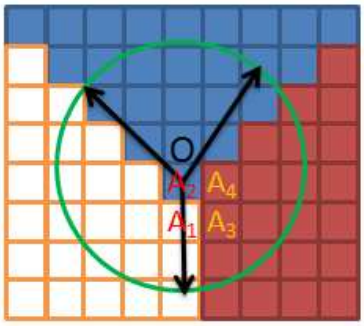

Figure 1: Schematic sketch of a trijunction in a voxel based microstructure representation. The grain regions of the 3 adjacent grains are indicated with different colors. The voxels labelled $A_1 \ldots A_4$ have all 3 different types of grains among their neighbors. The voxel labelled O is taken as the position of the triple junction. The dihedral angles are determined from the intersection of the grain boundaries with the green circle.

1. First the position of the grain boundaries and triple, quadruple and higher junctions is determined as described below. Consider for example the trijunction (Point O) in Fig. 1.
   (a) Extract the voxels for which $\sum_i \eta_i^2$ <=cutoff $\rightarrow P$. These voxels are all located at or near a grain boundary.
   (b) Examine for all voxels of P the four first-nearest and four second-nearest neighbors. It is assumed that a voxel belongs to a grain of type i if $\eta_i > \eta_j, \forall j \neq i$.
      i. If there are two different types of grains among the neighbors $\rightarrow G_{ij}$ (grain boundary between i^{th} grain and j^{th} grain)
      ii. If there are three different types of grains among the neighbors $\rightarrow T_{ijk}$ (trijunction where i^{th}, j^{th} and k^{th} grains coexist). If there are multiple voxels that meet this condition next to each other (for example the voxels A_1, A_2, A_3 and A_4 in Fig. 1), the $\sum_i \eta_i^2$ value is compared for the different voxels A_i and the voxel with the lowest value is taken as the position of the triple junction.
      iii. If there are four different types of grains among the neighbors $\rightarrow Q_{ijkl}$ (quadrijunction where i^{th}, j^{th}, k^{th} and l^{th} grains coexist). If multiple voxels next to each other meet this condition, the same selection process is performed as for the triple junctions.
      iv. If there are five different types of grains among the neighbors $\rightarrow P_{ijklm}$ (pentuple junction where i^{th}, j^{th}, k^{th}, l^{th} and m^{th} grains coexist). If multiple voxels next to each other meet this condition, the same selection process is performed as for the triple junctions.

v. If there are six different types of grains among the neighbors $\rightarrow H_{ijklmn}$ (hextuple junction where i^{th}, j^{th}, k^{th}, l^{th}, m^{th} and n^{th} grains coexist). If multiple voxels next to each other meet this condition, the same selection process is performed as for the triple junctions.

(c) If G_{ij} does not exist, T_{ijk} and T_{ijl} merge into Q_{ijkl}.
(d) If G_{ij} does not exist, T_{ijk} and Q_{ijmn} merge into P_{ijkmn}.
(e) If G_{ij} does not exist, T_{ijk} and P_{ijlmn} merge into H_{ijklmn}.

2. Draw a circle with its center at the multiple junction, for example the green circle around point O in Fig. 1
3. Find the intersection of the grain boundaries with the circle.
4. Calculate the coordinates of the vectors (black arrow) from the multiple junction to the intersections.
5. Calculate the angles between these vectors.

In our study, we chose the circle radius $r = 5$ in step 2. We examined the effect of taking various values for the radius of the circle and found that for $R = 1.00$ (isotropic structure) the peak of the dihedral angle distribution is sharpest for $r = 5$. We have also verified that the dihedral angle distributions for $R > 1.00$ did not change much when r is taken equal to 3, 5 or 7.

3.2. Measurement of grain boundary length

The line length measurement method for voxel based microstructure representation previously introduced in ref. [31] was based on the straight line assumption. This straight line assumption was reasonable for the study in ref. [31] because they considered systems with isotropic grain boundary energy and mobility. However, we found that the straight grain boundary assumption is inaccurate for grain structures with anisotropic grain boundary properties. Therefore, we introduce here an improved iterative method to measure the curved grain boundary length in voxel based microstructure representations generated by grain growth simulations of anisotropic systems.

An N-segment piecewise linear method (hereafter called N-SPLM) was implemented to measure the grain boundary length. The procedure is shown schematically in Fig. 2a and Fig. 2b. If the grain boundary is entirely straight, the line length can be evaluated by the distance between the two vertices (namely the distance between A and B in Fig. 2a and Fig. 2b. The voxels at the grain boundary region were sorted in ascending order of distance from the voxel A. Then, to measure the line length using a 2-SPLM, the voxel at the median rank was taken (C in Fig 2b) and the line length was calculated as the sum of the distances from A to C and C to B. This procedure was performed recursively and the curved boundary length was obtained from the n+1-SPLM if the difference of the lengths of n-SPLM and n+1-SPLM is less than 3%.

4. Simulations: Initial microstructure and general observations

Two different initial states were generated. From each state, simulations were started for the different R-values given in table 1. The initial states were

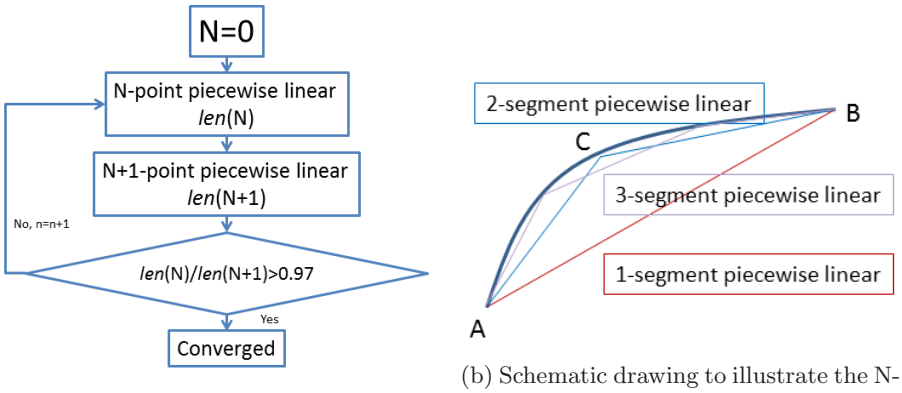

(a) Flow chart for the line length measurement using the N-segment piecewise linear method.

(b) Schematic drawing to illustrate the N-segment piecewise linear method applied to measure the grain boundary length between points A and B.

Figure 2: Flow chart and schematic drawing of the N-segment piecewise linear method to measure grain boundary length from a voxel based microstructure representation.

generated by an isotropic grain growth ($\theta_1 = \theta_2 = 1.0$) simulation starting from 20000 spherical grains distributed randomly in the system which were allowed to evolve until 3289 and 3270 grains remained, respectively. The remained order parameters were reassigned randomly to these grains and the grains labeled as η_i with i even were taken as α grains and those with i uneven as β grains. From this initial microstructure, anisotropic grain growth simulations were started using the different sets of $\theta_1 - \theta_2$ values listed in table 1. One of the initial states is shown in Fig. 3.

For all cases, a regime with steady-state grain growth behavior could be reached. We checked that the grain size distribution and the fraction of the two major vertice types did not notably change at the steady state, i.e. the fractions of trijunctions, quadrijunctions, etc did not vary more than 1% over 100 time steps during steady state growth. As R increases, the rate of grain elimination reduces and longer simulation times were required to obtain the steady-state. However, different from the growth stagnation observed for large R-values, namely for $R > \sqrt{3}$, in the previous Monte Carlo simulations [17], we achieved steady state growth and a steady state grain size distribution even for the large degrees of anisotropy. For R=3.10, we continued the simulation up to $12000\Delta t$, but did not observe any stagnation. The average grain diameter as a function of the square root of time is plotted in Fig. 4. For $\sqrt{t} > 100$, the remaining number of grains in the system has become too low to obtain reasonable statistics; although on average parabolic growth continues, the average mean grain size becomes more and more scattered. We believe, the stagnation observed in the Monte Carlo simulations [17] may have been due to artificial

lattice pinning. Probably, the dihedral angles at the quadruple junctions, which have values around 90°, could not be resolved appropriately on the triangular grid used in their simulations.

The simulated microstructures as observed in the steady-state regime for the different R-values are shown in Figs. 5a-5e. Pictures are taken at different times for different R-values such that the average grain size is similar. Although the amount of α and β type of grains is not a conserved property in the considered system, the fraction of the phases remains 0.5 throughout the simulations due to the symmetry in grain boundary properties.

5. Effect of anisotropy on the stability of different kinds of triple and quadruple junctions

The fractions of trijunction, quadrijuntion and higher junctions and the different types of them were determined from the simulated microstructures following the procedure described in section 3 and are listed in tables 2-4. For each R value, two simulations starting from a different initial state were performed and the fractions obtained in the 2 simulations were averaged. All quantities in the tables were measured at steady state. The fractions of two major vertice types did not notably change in the steady-state regime, i.e. their fractions did not vary more than 1% for $100\Delta t$.

$R = \sigma_{high}/\sigma_{low}$	Tri(%)	Quadri(%)	Quinque(%)	Sexa(%)
1.00	98.94	1.03	0.02	0.00
1.39	69.70	30.27	0.03	0.00
1.67	30.18	69.78	0.04	0.00
1.81	15.98	83.62	0.32	0.08
3.10	0.82	98.82	0.23	0.14

Table 2: Fractions of the trijunctions, quadrijunctions, quinquejunctions and sexajunctions for different R values measured from the simulated microstructures.

$R = \sigma_{high}/\sigma_{low}$	$t_{\alpha\alpha\alpha}/t_{\beta\beta\beta}(\%)$	$t_{\alpha\alpha\beta}/t_{\alpha\beta\beta}(\%)$
1.00	25	75
1.39	5	95
1.67	2	98
1.81	0	100
3.10	0	100

Table 3: Fractions of the two different types of the trijunctions at given R values. For each R value, two simulations starting from a different initial state were performed and the fractions obtained in the 2 simulations were averaged.

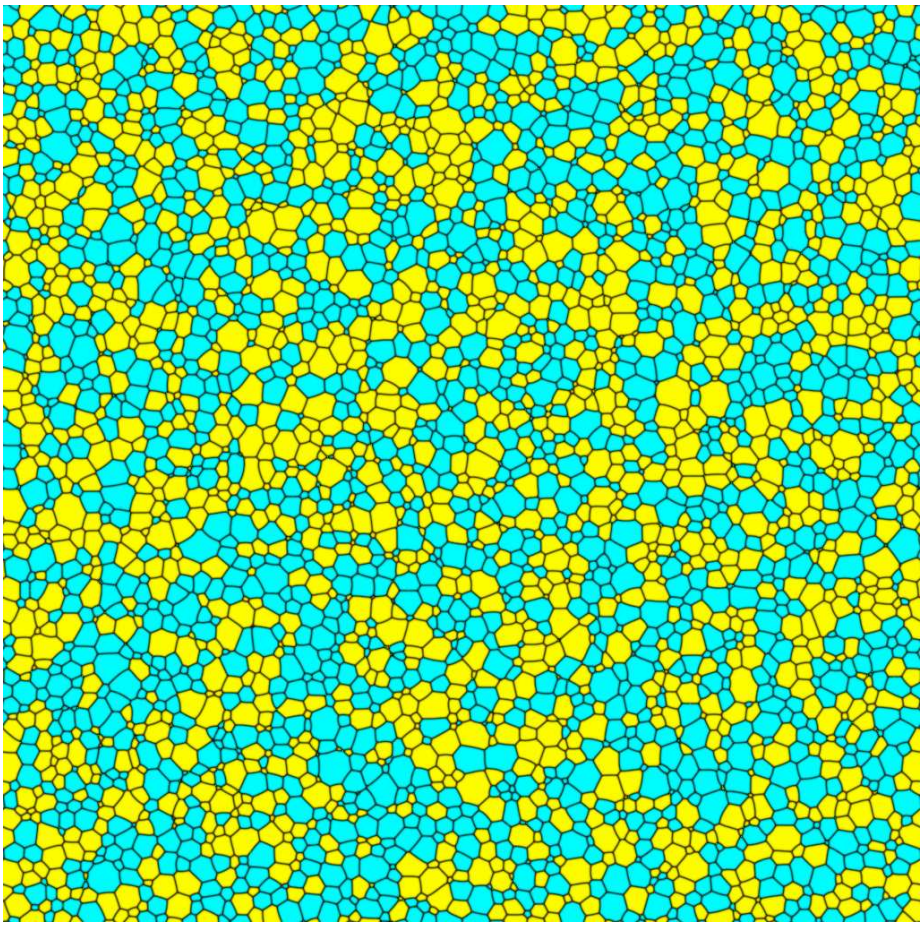

Figure 3: Representation of the microstructure used in this study as an initial state for the simulations. It was generated by an isotropic phase-field simulation. At the start 20,000 spherical grains were distributed randomly. The isotropic grain growth simulation was stopped when 3289 grains remained in the system. The microstructure is visualized by mapping the sum of the squared order-parameter values $\sum_i^Q \eta_i^2$ to a gray scale. The system size was 1024×1024 (expressed in voxels).The α grains and β grains are shown in cyan and yellow color, respectively.

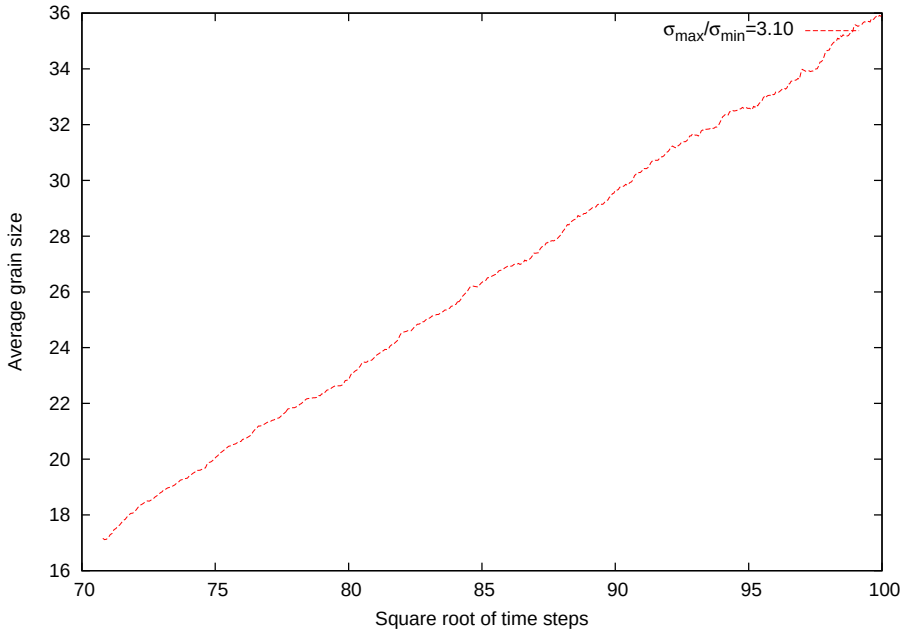

Figure 4: The average grain diameter (expressed in number of voxels) with respect to the square root of simulation time obtained for $R = 3.10$. The average grain diameter increases from 17.16 grid points to 35.91 grid points and the number of grains decreases from 3235 grains to 722 grains

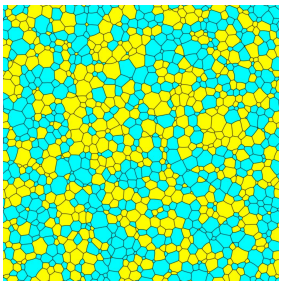

(a) $R = 1.00$: Obtained at 1500 Δt starting from the initial state. 1052 grains are still present in the system.

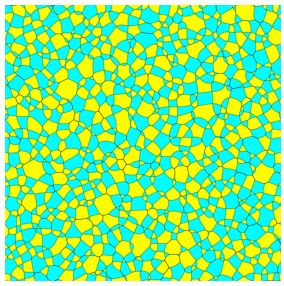

(b) $R = 1.39$: Obtained at $1500\Delta t$ starting from the initial state. 1005 grains are still present in the system.

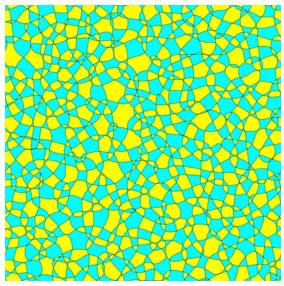

(c) $R = 1.67$: Obtained at $2000\Delta t$ starting from the initial state. 1072 grains are still present in the system.

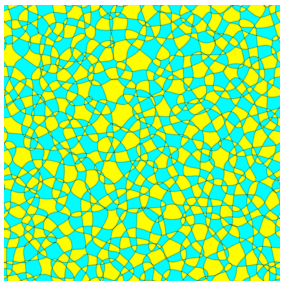

(d) $R = 1.81$: Obtained at $3000\Delta t$ starting from the initial state. 1160 grains are still present in the system.

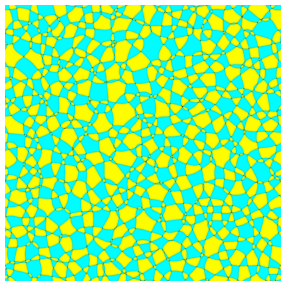

(e) $R = 3.10$: Obtained at $3000\Delta t$ starting from the initial state. 1160 grains are still present in the system.

Figure 5: Simulated microstructures obtained during steady-state growth for different degrees of anisotropy, namely for $R = 1$, 1.39, 1.67, 1.81 and 3.10. The system size was 1024×1024 (expressed in voxels). The α grains and β grains are shown in cyan and yellow color, respectively.

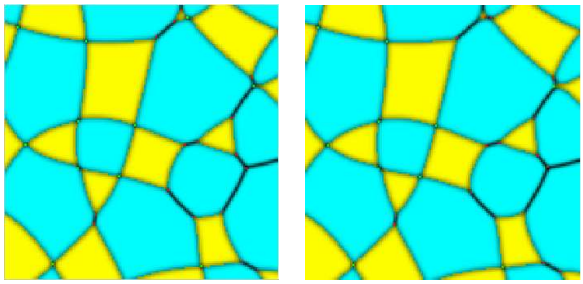

(a) $R = 1.39$. At $6500\Delta t$: (b) $R = 1.39$. At $6520\Delta t$

Figure 6: Highly magnified part of the simulated microstructures obtained at 2 different time steps for $R = 1.39$. The α grains and β grains are described by cyan color and yellow color. A red spot indicates a trijunction and a green spot a quadrijunction. Comparison of the figures (a) and (b) shows that the quadrijunctions on the left and in the center do not immediately decompose into trijunctions. On the other hand, the quadrijunction in the right top part of Fig.6a at $6500\Delta t$ has split into two trijunctions in Fig.6b at $6520\Delta t$.

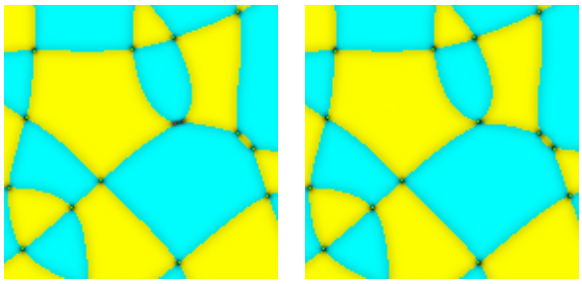

(a) $R = 3.10$. At $8500\Delta t$ (b) $R = 3.10$. At $8520\Delta t$

Figure 7: Highly magnified part of the simulated microstructures obtained at 2 different time steps for $R = 3.10$. The α grains and β grains are described by cyan color and yellow color. A red spot indicates a trijunction and a green spot a quadrijunction. The 2 trijunctions seen in Fig. 7a at $8500\Delta t$ have merged into 1 quadruple junction in Fig. 7b.

$R = \sigma_{high}/\sigma_{low}$	$q_{\alpha\alpha\alpha\alpha}/q_{\beta\beta\beta\beta}(\%)$	$q_{\alpha\alpha\alpha\beta}/q_{\alpha\beta\beta\beta}(\%)$	$q_{\alpha\beta\alpha\beta}(\%)$
1.00	6.98	55.81	37.21
1.39	0.00	3.60	96.40
1.67	0.00	0.46	99.54
1.81	0.00	0.47	99.53
3.10	0.00	0.50	99.50

Table 4: Fractions of the three different types of quadrijunctions at given R values. For each R value, two simulations starting from a different initial state were performed and the fractions obtained in the 2 simulations were averaged.

As predicted by Cahn, Holm and Srolovitz [16, 17], we rarely observed quadrijunctions or higher junctions in the microstructure with isotropic grain boundary properties. As given in table 2, the fraction of quadri- and higher junctions was approximately 1.05% for $R = 1.00$. Furthermore, according to table 3, the fraction of $t_{\alpha\alpha\alpha}/t_{\beta\beta\beta}$ type junctions among all trijunctions was 25% for $R = 1$, which is also consistent with the simple probabilistic prediction for the possibility to form $t_{\alpha\alpha\alpha}/t_{\beta\beta\beta}$ type trijunctions are $\frac{2}{2\times2\times2} = 0.25$.

Although according to the predictions of Cahn, Holm and Srolovitz [16, 17], quadruple junctions are expected to become stable only for $R \leq \sqrt{2}$, the fraction of quadri- and higher junctions was approximately 30.0% of the total vertice count in the simulations for $R = 1.39 < \sqrt{2}$, which is already much higher than for $R = 1.00$. Moreover, from the consecutive images in Figs 6a and 6b, it is clear that most of the quadrijunctions can exist for a considerable time and can thus be considered as being stable. The theoretical predictions of Cahn, Holm and Srolovitz's assumed however straight grain boundaries [16, 17], whereas in real microstructures most grain boundaries are curved, which may slightly affect the stability of the junctions. Moreover, the value of 1.39 is very close to $\sqrt{2} \approx 1.41$. In agreement with the theoretical prediction both types of triple junctions are stable. The majority of the triple junctions is however of the type $t_{\alpha\alpha\beta}/t_{\alpha\beta\beta}$, since $\sigma_{\alpha\beta} < \sigma_{\alpha\alpha} = \sigma_{\beta\beta}$ and therefore grains of different types have the tendency to alternate, as was also observed in previous Monte Carlo simulations [17].

In the simulations with $R = 1.67$, the major kind of vertices was the $q_{\alpha\beta\alpha\beta}$ type quadrijunction. There were also still a considerable amount of triple junctions. This is in agreement with the theoretical predictions of Cahn [16], since, for $\sqrt{2} \leq R = 1.67 \leq \sqrt{3}$, it is namely expected that both types of trijunctions and the $q_{\alpha\beta\alpha\beta}$ type of quadrijunction are stable. As in the previous case, the fraction of $t_{\alpha\alpha\alpha}/t_{\beta\beta\beta}$ type of triple junctions is quite low, namely less than 4%, since α and β grains have the tendency to alternate for $\sigma_{\alpha\beta} < \sigma_{\alpha\alpha} = \sigma_{\beta\beta}$.

When $R = 1.81 > \sqrt{3}$ in the simulations, more than 81% of the vertices are quadrijunctions and more than 99% of them are of $q_{\alpha\beta\alpha\beta}$ type. The major type of triple junctions is $t_{\alpha\alpha\beta}/t_{\alpha\beta\beta}$. This is in agreement with the predictions of Cahn [16] for $\sqrt{3} < R < 2$.

If $R = 3.10 > 2.0$, more than 98% of the junctions are $\alpha\beta\alpha\beta$-typed quadrijunctions in the simulations. Triple junctions can form, however they appear to

be unstable. In Fig. 7a, for example, one can see two trijunctions located close to each other in a simulated microstructure for $R = 3.10$. However, they merge into one quadrijunction within less then $20\Delta t$ as shown in Fig.7b. This is in agreement with the prediction of Cahn, Holm and Srolovitz which says that the $q_{\alpha\beta\alpha\beta}$ quadrijunction is the only stable vertice type when $R >= 2$.

In general our observations show thus good agreement with the trends predicted by Cahn, Holm and Srolovitz [16, 17]. The junction types that are unstable in the predictions by Cahn, Holm and Srolovitz's analysis are always found to be a minor junction type in the simulations, although in some cases we can still detect them in the system.

6. Distributions of dihedral angles, number of faces, normalized grain size and normalized grain boundary length

6.1. Dihedral angles

The equilibrium dihedral angles at triple junctions are fixed and can be calculated easily as a function of the magnitude of the grain boundary anisotropy from an interfacial tension balance (Lami's theorem). The $t_{\alpha\alpha\alpha}/t_{\beta\beta\beta}$ type of triple junction is accordingly expected to have all 3 dihedral angles equal to 120° and the $t_{\alpha\alpha\beta}/t_{\alpha\beta\beta}$ type of triple junction is expected to have 2 angles equal to $\pi - \arccos(R/2)$ and 1 angle equal to $2\arccos(R/2)$. Therefore, a distribution with sharp peaks at the possible equilibrium dihedral angles is expected if only triple junctions are present. The equilibrium dihedral angles at quadruple junctions however are not uniquely determined by an interfacial tension balance. Assuming grain boundaries are straight and behave independent from the rest of the grain boundary network, Cahn calculated a lower and higher bound between which the dihedral angles at a stable quadruple junction may vary, with the lower bound given by $\Phi_l \geq 2\arccos(R/2)$ and the higher bound by $\Phi_h \leq \pi - \Phi_l$. As discussed before and shown in figure 6, in connected grain structures it is possible that quadruple junctions with an angle outside this range become stable as well, although it is a minority event. Consequently, one cannot easily deduce how the degree of anisotropy will affect the distribution of dihedral angles when quadruple junctions become stable.

The distributions of the dihedral angles as obtained from the simulations for different magnitudes of the anisotropy R are shown in Figs. 8a-8d. For each case, it is shown how the dihedral angles at the triple and quadruple junctions separately contribute to the total distribution of dihedral angles.

When $R = 1$ (Fig. 8a), there are only triple junctions and the dihedral angle distribution peaks at 120°, as expected in the case of isotropic grain boundary properties [32, 33].

When $R = 1.39$, the majority (70%) of junctions is still a trijunction (see table 2) and most of them are of the $t_{\alpha\alpha\beta}/t_{\alpha\beta\beta}$ type. The contribution from the trijunctions in Fig. 8b (blue curve) shows two peaks, one around 70°-80° and another around 150°, which deviates from the equilibrium angles 91.95° and 134.03° calculated from Lami's theorem for the $t_{\alpha\alpha\beta}/t_{\alpha\beta\beta}$ type of triple

junction and $R = 1.39$. To verify that the deviation of the triple junction angles from their equilibrium value is not due to the modeling approach or a numerical artifact, a grain growth simulation was performed considering a system with 3 grains as shown in Fig. 9. The grain boundary energy of the boundary between the yellow and cyan grains is 1.39 times higher than that of the boundaries between the yellow and red grains and the yellow and cyan grains. In this simulation, dihedral angles at the triple junction were equal to 90° and 135° which is very close to the equilibrium angles (the deviation is less than 2%). It was also shown by Tang et al. [25] that the implemented phase field model is able to reproduce dihedral angles in highly anisotropic systems accurately. Therefore, we conclude that the observed deviation from equilibrium in the simulations for $R = 1.39$ is because of topological restrictions imposed by the surrounding grain network. A closer look at the microstructure namely shows that the $t_{\alpha\alpha\beta}/t_{\alpha\beta\beta}$ triple junctions are most often at rather small triangular grains which often exist per two with two triple junctions and a grain boundary in between, as shown in Fig. 10. Highly curved grain boundaries at these triangular grains would thus be required to obtain the equilibrium dihedral angles in the triple junctions. Moreover, the large driving force to shorten the high energy α-α or β-β grain boundary connecting the 2 triangular grains also prevents the dihedral angles at the triangular grains to obtain their equilibrium values. Consequently, the surfaces of the triangular grains are only weakly convex during grain evolution and the inner angles of the 2 triangles are an angle Δ sharper than expected, i.e. 92°-Δ, while the 2 outer angles are an angle $\Delta/2$ larger than expected, i.e. 134°+$\Delta/2$. There is a wide spread on the value of Δ depending on the surrounding grain boundary network. The distribution of the quadruple junctions (green curve) peaks at 90°, but the angles vary within a wide range. In the total distribution, the peaks from the trijunction angles distribution are still present, however the peak around 67.4° is smeared out due to the contribution from the quadrijunction angles.

For $R = 1.67$ (Fig. 8c), almost 70% of the junctions are $q_{\alpha\beta\alpha\beta}$ junctions. The overall distribution of the dihedral angles in Fig. 8c has accordingly a broad peak around 90° (red line). The curve of the triple junction dihedral angles shows two peaks, one around 50° and a broad peak around 160°. Also in this case the $t_{\alpha\alpha\beta}/t_{\alpha\beta\beta}$ triple junction angles of the evolving microstructure deviate from their equilibrium values and are determined by the topological restrictions imposed by the surrounding network. On average, the deviation of the triple junction angles from their equilibrium values is larger than for the case $R = 1.39$ since the driving force to shorten the high energy boundary in between 2 triangular grains is larger. For $R = 1.81$ and $R = 3.10$, quadrijunctions are dominant (see table 2) and the dihedral angle distribution has a wide peak at 90°, as shown in Figs. 8d and 8e.

6.2. Number of faces

The distributions of the number of phases obtained for different R-values are plotted in Fig. 11. As predicted by the former works [37, 38], the distribution of the number of faces has a peak at $f = 6$ for the isotropic case ($R = 1.00$) in

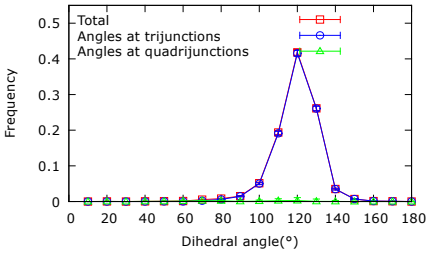

(a) $R = 1.00$. At $1500\Delta t$ from the initial state.

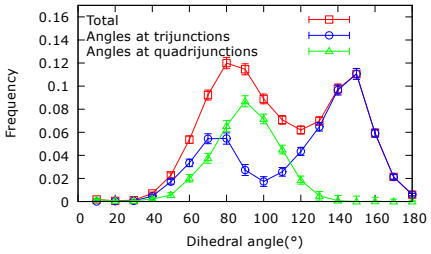

(b) $R = 1.39$. At $1500\Delta t$ from the initial state.

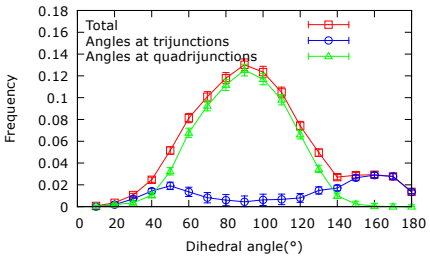

(c) $R = 1.67$. At $2000\Delta t$ from the initial state.

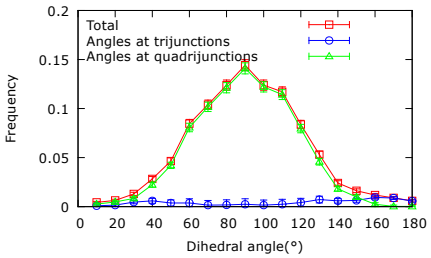

(d) $R = 1.81$. At $3000\Delta t$ from the initial state.

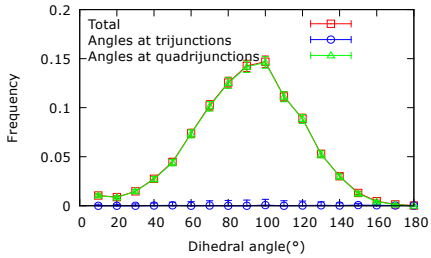

(e) $R = 3.10$. At $3000\Delta t$ from the initial state.

Figure 8: The distribution of the dihedral angles at the scaling regime obtained in the simulations for different R-values.

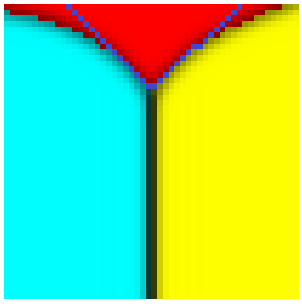

Figure 9: Grain geometry used to verify the equilibrium dihedral angles at triple junctions obtained in the simulated systems. The energy of the grain boundary between the yellow and cyan grains is 1.39 times higher than that of the grain boundary between the yellow and red grains and that between the yellow and cyan grains. The blue lines indicate the tangential to the grain boundary at the triple junction.

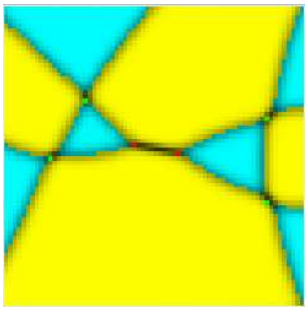

Figure 10: Highly magnified region of the microstructure obtained for $R = 1.39$ showing the typical triangular grains with non-equilibrium dihedral angles present in this microstructure. The α grains and β grains are described by cyan color and yellow color.

our study. For all other cases ($R = 1.39, 1.67, 1.81, 3.10$), the distribution of the number of faces has a peak at $f = 3$. The distributions of the number of faces have a very similar shape when $R = 1.67, 1.81$ and 3.10, where the majority of the junctions are quadruple. There is a peak at $f = 3$, but there is also a large amount of grains with 4 sides. For $R = 1.39$, where both triple and quadruple junctions are present, the distribution is much broader and the number of 3-sided, 4-sided and 5-sided grains is comparable even though the distribution is peaked at $f = 3$.

Since, the dihedral angles at quadrijunctions are not thermodynamically fixed [17], it is not intuitive how to relate the distributions of the dihedral angles and the vertex types with that of the number of faces. In the trijunction dominant system, the hexagonal grain (6-sided) is the most frequent type of grains and the second frequent type of grain is the pentagonal grain (5-sided) [37, 38]. Therefore, we can conclude that trijunctions seem to favor 5 and 6-sided grains and quadruple junctions 3- and 4-sided grains. Cahn, Holm and Srolovitz predicted the presence of the 3-sided and 4-sided ZIC grain which has Zero Integrated Curvature in quadrijunction dominant systems [17].

As shown in Fig. 12a and Fig. 12b, if one 3-sided grain is eliminated (the grain surrounded by the violet circle), the surrounding 4-sided or 5-sided grains also lose one of their sides (yellow). As a result, two 3-sided grains (yellow) and one 4-sided grain are generated from the removal of one 3-sided (cyan) grain. It can be a reasonable explanation why the number of 3-sided grains is higher than that of 4-sided grains for $R >= 1.39$.

We also note that, while 2-sided grains do not exist in the isotropic case, there is a small fraction of 2-sided grains present in anisotropic systems with quadruple junctions. Two-sided grains were also noticed in phase field simulations of the evolution of conserved two-phase systems with quadruple junctions [36]

6.3. Normalized grain size

The normalized grain size distribution for different magnitudes of anisotropy is plotted in Figs. 13a to 13e. The individual contributions from the different topological classes are plotted as well. The distributions are plotted at one particular time step in the steady-state regime, however it was verified that the distributions did not change considerably once steady-state growth is reached. According to Fig. 13a, for $R = 1.00$ the three distribution profiles of the major topological classes ($f = 5$,$f = 6$ and $f = 7$) form a distribution with a plateau as was also pointed out by Kim et al. [7] for systems with isotropic grain boundary energy and mobility. For increasing magnitude of the anisotropy R, the contributions from grains with 3 and 4 sides become more significant (see Figs 13b to 13e) and affect the shape of the grain size distribution. As can be seen in Fig. 13d for $R = 1.81$, peaks, mainly formed by the contributions from the 3- and 4-sided grains, are initiated on the plateau. When $R = 3.10$ (see Fig. 13e), a bimodal grain size distribution has clearly develop, with the left peak mainly coming from the 3-sided grains and the right peak from the 4-sided grains. Although it is generally accepted that a bimodal grain size distribution is a significant evidence of abnormal grain growth [34, 35], in our anisotropic

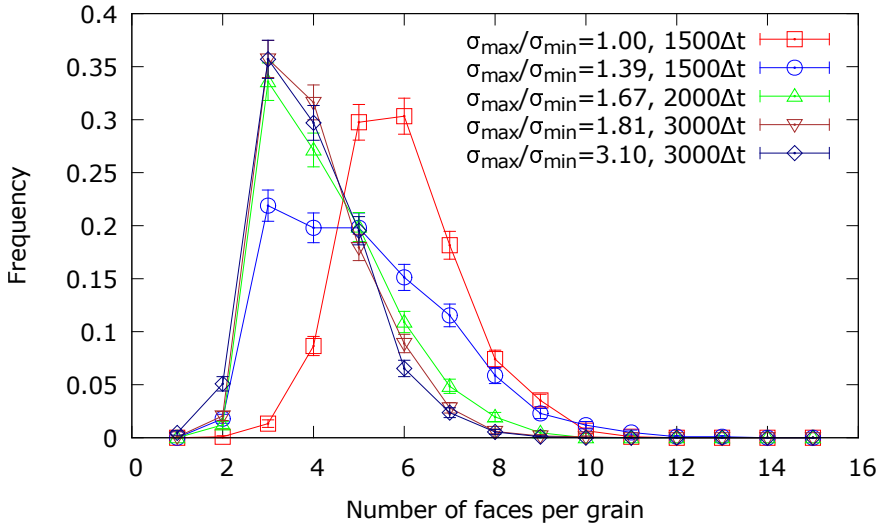

Figure 11: The distribution of the number of faces at the steady-state regime for $R = 1.00$ (red), $R = 1.39$ (blue), $R = 1.67$ (green), $R = 1.81$ (brown) and $R = 3.10$ (navy). The grain size distributions were plotted at $1500\Delta t$ from the initial state for $R = 1.00, 1.39$, at $2000\Delta t$ from the initial state for $R = 1.67$ and at $3000\Delta t$ from the initial state for $R = 1.81, 3.10$.

grain growth simulation, the bimodal grain size distribution is observed without implementation of any abnormality. It is because the 3-sided and 4-sided grains form the major two peaks of the bimodal distribution. Moreover, it is invariant in time.

6.4. Normalized grain boundary length

The distributions of the normalized grain boundary lengths are plotted in Fig. 14 for different R-values. The distributions obtained for $R = 1.39, 1.81$ and 3.1, where a considerable amount of quadruple junctions are present, are much broader than that obtained for the isotropic case ($R = 1.00$).

7. Conclusion

Two-dimensional phase-field simulations were performed of grain growth in highly textured materials with equal fractions of 2 texture components and assuming 2 values of the grain boundary energy, namely σ_{low} for boundaries between grains of a different orientation and σ_{high} for boundaries between grains of a similar orientation. For $R = \sigma_{high}/\sigma_{low} > 1$, the simulated structures consisted of alternating α and β grains. Different from the growth stagnation observed for large R-values in previous Monte Carlo simulation, we achieved steady-state growth even for high degrees of anisotropy (i.e. large R-value).

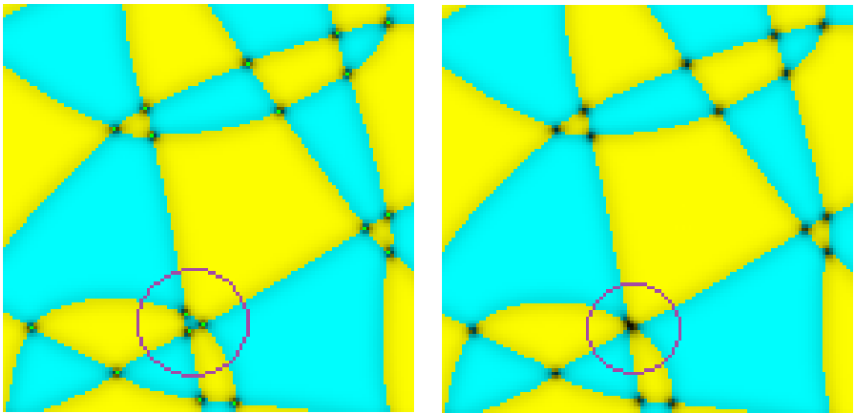

(a) 3500 Δt ahead from the initial state.

(b) 3560 Δt ahead from the initial state.

Figure 12: $R = 3.10$. Highly magnified region of the microstructure. The α grains and β grains are described by cyan color and yellow color and a green spot indicates a quadrijunction. A disappearing 3-sided grain is indicated with a violet circle. As a result, two 4-sided grains transform into a 3-sided grain, whereas only one 5-sided grain transforms into a 4-sided grain.

Quadruple junctions were already stable from $R = 1.39$, which is a slightly lower value than the $R = \sqrt{2}$ predicted by Cahn, Holm and Srolovitz. However, in general, our observations were consistent with the predictions of Cahn Holm and Srolovitz [16, 17].

We found that the presence of quadruple junctions has a large effect on the steady-state shape of the distributions of the grain sizes, the number of faces, the dihedral angles at junctions and the grain boundary length. The main findings are the following:

- Since quadruple junctions are thermodynamically not fixed, the distribution of the dihedral angles has a broad peak around 90° for $R \geq 1.67$, when most of the junctions are of the $q_{\alpha\beta\alpha\beta}$ quadruple type, whereas a sharp peak at 120° is generally obtained in the isotropic case.

- For $1 < R < 1.67$, when both triple and quadruple junctions are stable, the distribution of the dihedral angles can have multiple peaks coming from the different types of triple and quadruple junctions. However, due to geometrical restrictions imposed by the surrounding grain boundary network, the triple junctions generally deviate from the equilibrium dihedral angles.

- The distribution of the number of faces peaks at $f = 6$ for $R = 1$, where only triple junctions are present, and at $f = 3$ for $R \geq 1.67$, when the majority of the junctions are of the quadruple type. Once $R \geq 1.67$, very

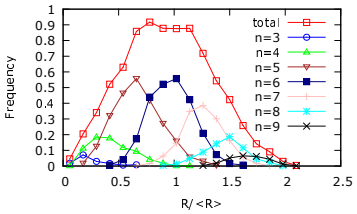

(a) $R = 1.00$. Taken at 1500 Δt ahead from the initial state. The major three topological classes are n=5, n=6 and n=7.

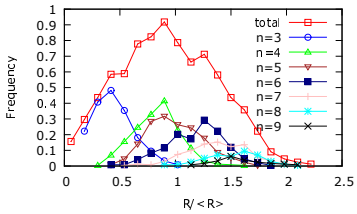

(b) $R = 1.39$. Taken at 1500 Δt ahead from the initial state.The major four topological classes are n=3, n=4, n=5 and n=6.

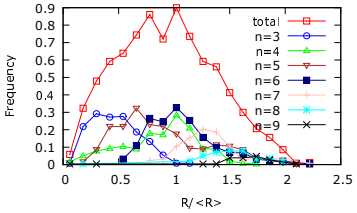

(c) $R = 1.67$. Taken at 2000 Δt ahead from the initial state. The major four topological classes are n=3, n=4, n=5 and n=6.

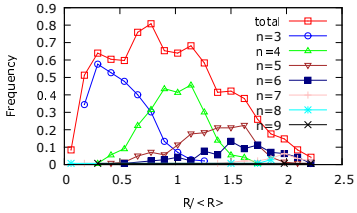

(d) $R = 1.81$. Taken at 3000 Δt ahead from the initial state. The major two topological classes are n=3 and n=4.

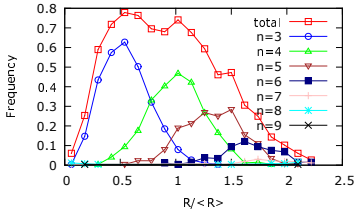

(e) $R = 3.10$. Taken at 3000 Δt ahead from the initial state. The major two topological classes are n=3 and n=4.

Figure 13: The overall steady-state normalized grain size distributions and contributions from each topological class for different R values. The data were collected from two different sets of simulations to obtain more rigorous statistics.

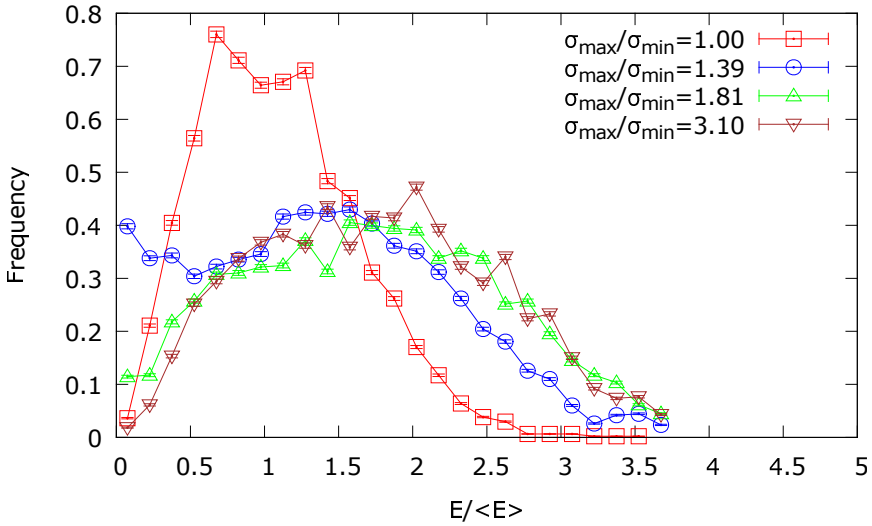

Figure 14: The distribution of the normalized grain boundary length at the scaling regime for $R = 1.00$ (red), $R = 1.39$ (blue), $R = 1.81$ (green) and $R = 3.10$ (brown). The distributions were taken at $1500\Delta t$ after the initial state for $R = 1.00$ and 1.39 and at $3000\Delta t$ after the initial state for $R = 1.81$ and 3.10. E represents the grain boundary length of each grain boundary and $< E >$ the average grain boundary length.

similar distributions are obtained for simulations with different R-values. For $R = 1.39$, where both triple and quadruple junctions are present, a broad distribution is found, which however peaks at $f = 3$.

- For high degree of anisotropy, where only quadruple junctions are stable, a bimodal grain size distribution is obtained, but it does not lead to abnormal grain growth.

Acknowledgements: We sincerely appreciate the CREA-financing of KU Leuven, grant CREA/12/012 on Phase field modeling of the morphological evolution during phase transitions in organic materials. Parallel simulations were run on the High Performance Computer cluster of VSC (Vlaams Supercomputer Centrum).

References

[1] Hall EO. Proc Phys Soc 1951;64B:747

[2] Petch NJ. J Iron Steel Inst 1953;174:25

[3] Iwai H, Naoki S, Matsui T, Teshima H, Kishimoto M, Kishida R, Hayashi D, Matsuzaki K, Kanno D, Saito M, Muroyama H, Eguchi K, Kasagi N, Yoshida H. Jour of Pow Sou 2010;195:955

[4] Wang L, Zhang J, Gao Y, Xue Q, Hu L, Xu T. Scripta Mat 2006;55:657

[5] Chen LQ, Yang W. Phys Rev B 1994;50:15752

[6] Srolovitz DJ, Anderson MP, Sahni PS, Grest GS. Acta Metall 1984;32:793

[7] Kim SG, Kim DI, Kim WT, Park YB. Phys Rev E 2006;74:061605

[8] Rollett AD, Srolovitz DJ, Anderson MP. Acta Metall 1989;37:1227

[9] Gruber J, Miller HM, Hoffmann TD, Rohrer GS, Rollett AD. Acta Mater 2009;57:6102

[10] Kazaryan A, Wang Y, Dregia SA, Patton BR. Acta Mater 2002;50:2491

[11] Johnson OK, Schuh CA. Acta Mater 2013;61:2863

[12] Horn JA, Zhang SC, Selvaraj U, Messing GL, Trolier-McKinstry S. J Am Ceram Soc 1999;82:921

[13] Seabaugh MM, Kerscht IH, Messing GL. J Am Ceram Soc 1997;80:1181

[14] Ivasishin OM, Shevchenko SV, Semiatin SL. Script Mater 2004;50:1241

[15] Abbruzzese G, Lücke K. Acta Metall 1986;34:905

[16] Cahn JW. Acta Metall 1991;39:2189

[17] Holm EA, Srolovitz DJ, Cahn JW. Acta Metall 1993;41:1119

[18] Gertsman VY. Interface Sci 1999;7:231

[19] He ZB, Stolitchnova I, Settera N, Cantonib M, Wojciechowski T, Karczewski G. J Alloys Compd 2009;484:757

[20] Poulsen SO, Voorhees PW, Lauridsen EM. Acta Mater 2013;61:1220

[21] Ma N, Kazaryan A, Dregia SA, Wang Y. Acta Mater 2004;52:3869

[22] Kazaryan A, Patton BR, Dregia SA, Wang Y. Acta Mater 2002;50:499

[23] Holm EA, Hassold GN, Miodownik MA. Acta Mater 2001; 49:2981

[24] Moelans N, Blanpain B, Wollants P. Phys Rev B 2008;78:024113

[25] Tang M, Reed BW, Kumar M. J Appl Phys 2012;112;043505

[26] Vanherpe L, Moelans N, Blanpain B, Vandewalle S. Phys Rev E 2007;76:056702

[27] Vanherpe L, Moelans N, Blanpain B, Vandewalle S. Comp Mater Sci 2011;50:2221

[28] Chen LQ, Shen J. Comp Phys Comm 1998;108:148

[29] Vedantam S, Patnaik BSV. Phys Rev E 2006;73:016703

[30] Gruber J, Ma N, Wang Y, Rollett AD, Rohrer GS. Model Simul Mater Sci Eng 2006;14:1189

[31] Chang K, Krill CE III, Du Q, Chen LQ. Model Simul Mater Sci Eng 2012;20:075009

[32] Neumann JV. In: Metal interfaces. American Society for Testing Materials, Cleveland, 1952:108

[33] Mullins WW. J Appl Phys 1956;27:900

[34] Thompson CV, Frost HJ, Spaepen F. Acta Metall 1987;35:887

[35] MacLaren I, Cannon RM, Gülgün MA, Voytovych R, Popescu-Pogrion N, Scheu C, Täffner U, Rühle. M J Am Ceram Soc 2003;86:650

[36] Fan D, Chen LQ. Scripta Mater 1997;37:233

[37] Saito Y. Mat Sci Eng A 1997;A223:114

[38] Gill S, Cocks A. Acta Mate 1996;44:4777